INTERNATIONAL JOURNAL FOR NUMERICAL AND ANALYTICAL METHODS IN GEOMECHANICS
Int. J. Numer. Anal. Meth. Geomech., 2003; **27**:1277–1297 (DOI: 10.1002/nag.320)

Application of unconstrained optimization and sensitivity analysis to calibration of a soil constitutive model

Zhaohui Yang*,† and Ahmed Elgamal‡

Department of Structural Engineering, U.C. San Diego, La Jolla, CA 92093, U.S.A.

SUMMARY

Large sets of soil experimental data (field and laboratory) are becoming increasingly available for calibration of soil constitutive models. A challenging task is to calibrate a potentially large number of model parameters to satisfactorily match many data sets simultaneously. This calibration effort can be facilitated by optimization techniques. The current study aims to explore systematic approaches for exercising optimization and sensitivity analysis in the area of soil constitutive modelling. Analytical, semi-analytical and numerical optimization techniques are employed to calibrate a multi-surface-plasticity sand model. Calibration is based on results from a number of drained triaxial sample tests and a dynamic centrifuge liquefaction test. The analytical and semi-analytical approaches and associated sensitivity analysis are applied to calibrate the model non-linear shear stress–strain response. Thereafter, model parameters controlling shear–volume coupling effects (dilatancy) are calibrated using a solid–fluid fully coupled finite element program in conjunction with an advanced numerical optimization code. A related sensitivity study reveals the challenges often encountered in optimizing highly non-linear functions. Overall, this study demonstrates applicability and limitations of optimization techniques for constitutive model calibration. Copyright © 2003 John Wiley & Sons, Ltd.

KEY WORDS: optimization; sensitivity; liquefaction; constitutive modelling; soil plasticity

1. INTRODUCTION

In order to simulate pressure-dependent soil response under complex cyclic loading conditions, soil constitutive models typically include a large number of parameters. Recently, soil experimental data sets (field and laboratory) are becoming increasingly available for calibration of such constitutive models. Thus, a challenging task is to calibrate a potentially large number of model parameters to satisfactorily match many data sets simultaneously. In this regard,

*Correspondence to: Zhaohui Yang, Department of Structural Engineering, U.C. San Diego, La Jolla, CA 92093, U.S.A.
† E-mail: zhyang@ucsd.edu
‡ E-mail: elgamal@ucsd.edu

Contract/grant sponsor: National Science Foundation; contract/grant number: CMS-9416248
Contract/grant sponsor: Pacific Earthquake Engineering Research (PEER) Center; contract/grant number: EEC-9701568

systematic and convenient calibration is most valuable towards successful application of these soil models [1–7].

The calibration effort can be facilitated by optimization techniques. An optimization procedure systematically searches for a set of model parameters that can simultaneously minimize the difference between a large number of experimental records and the corresponding model simulation results. In simple cases, closed-form solutions to an optimization problem may exist so that an optimized set of parameters can be obtained analytically. In more general cases, one has to resort to a numerical optimization algorithm [8–13]. Indeed, efforts have been reported in development of efficient optimization algorithms, and their applications to the areas of soil constitutive model calibration (e.g. References [1, 2, 4–6]), and geotechnical system identification (e.g. References [3, 7, 14–17]).

In this paper, analytical, semi-analytical and numerical optimization techniques were employed to calibrate a multi-surface-plasticity sand model [18, 19], for Nevada sand at 40% relative density (D_r). Analytical and semi-analytical approaches and associated sensitivity analysis were applied to calibrate the model non-linear shear stress–strain response (backbone-curve). Experimental data involved in this part of the calibration include results from a set of drained triaxial tests on Nevada sand at about 40% initial D_r [20]. In addition, optimization results for 60% D_r Nevada sand are presented for comparison. Thereafter, model parameters controlling shear–volume coupling effects (dilatancy) were calibrated using a solid–fluid fully coupled finite element program in conjunction with an existing numerical optimization computer code. Experimental data involved in this part of the calibration was from a centrifuge liquefaction experiment, in which the same Nevada sand was employed at about 40% initial D_r [21]. Finally, a sensitivity analysis was conducted to explore complexities often encountered in optimizing highly non-linear functions.

In the following sections, the employed concepts of unconstrained optimization and sensitivity analysis are introduced. The essential elements of the soil constitutive model and modelling parameters involved in the optimization process are summarized. This is followed by a presentation of the model calibration process and its outcome, along with results of the sensitivity analyses.

2. UNCONSTRAINED OPTIMIZATION BACKGROUND

Optimization problems can be stated as [10, 12]: Find a set of parameters $\mathbf{x}$ such that a scalar objective function $f(\mathbf{x})$ is minimized. In the context of model calibration, $f(\mathbf{x})$ is a scalar measure of the 'goodness' of a model. One example is to define $f(\mathbf{x})$ using the well known least squares method, which minimizes the sum of squares of the difference between mathematical model predictions and observations:

$$f(\mathbf{x}) = \sum_{i=1}^{N} (Y_i(\mathbf{x}) - y_i)^2 \tag{1}$$

where $Y_i(\mathbf{x})$ is model prediction at a certain time and/or location i, y_i the corresponding observation, and N the total number of observation points. It is emphasized that optimization is meaningful only if the model predictions $\mathbf{Y}(\mathbf{x})$ describe adequately the essential physical

mechanism(s) underlying the observed response y. By minimizing $f(\mathbf{x})$, one finds the 'best' set of model parameters $\mathbf{x}^*$ to match the available data.

The undetermined parameters $\mathbf{x}$ are often subject to certain constraints on the range of values they can assume. In this paper, only simply bounded problems are considered (i.e. $\mathbf{l} \leqslant \mathbf{x} \leqslant \mathbf{u}$, where $\mathbf{l}$ and $\mathbf{u}$ are constants defining lower and upper bounds), and most in fact degrade to the unconstrained case (i.e. optimal values $\mathbf{x}^*$ are not on either bound). Therefore, discussions hereafter will focus only on unconstrained optimization.

Assuming $f(\mathbf{x})$ twice-continuously differentiable, the first derivative (i.e. the gradient) and the second derivative (known as the Hessian) of $f(\mathbf{x})$ are given by

$$\mathbf{g}(\mathbf{x}) \equiv \frac{\partial f}{\partial \mathbf{x}}, \quad \mathbf{H}(\mathbf{x}) \equiv \frac{\partial^2 f}{\partial \mathbf{x}^2} \tag{2}$$

It is often desirable to normalize the above gradients so as to be independent of the physical units of $\mathbf{x}$:

$$\mathbf{g}(\mathbf{x})^{\text{normlized}} \equiv \mathbf{Q} \cdot \mathbf{g}(\mathbf{x}), \quad \mathbf{H}(\mathbf{x})^{\text{normlized}} \equiv \mathbf{Q} \cdot \mathbf{H}(\mathbf{x}) \cdot \mathbf{Q} \tag{3}$$

where $\mathbf{Q} = \text{diag}(1/X_1, \ldots, 1/X_N)$ is a diagonal matrix of appropriate normalization constants $X_1, \ldots, X_N$ (e.g. the optimal parameter values $\mathbf{x}^*$).

Sufficient conditions for a minimum in an unconstrained optimization problem are [10, 12]: $\mathbf{g}(\mathbf{x}^*) = 0$ (i.e. $\mathbf{x}^*$ is a stationary point), and $\mathbf{H}(\mathbf{x}^*)$ is positive definite. Depending on the availability and complexity of $\mathbf{g}$ and $\mathbf{H}$, a minimum point $\mathbf{x}^*$ may be found by using one of the following three general approaches [2]:

(1) Zero-order method: requires evaluations of $f(\mathbf{x})$ only, and no information about $\mathbf{g}$ or $\mathbf{H}$ is needed [6].
(2) First-order method: requires evaluations of $f(\mathbf{x})$ as well as $\mathbf{g}(\mathbf{x})$. If $\mathbf{g}(\mathbf{x})$ are simple functions, $\mathbf{g}(\mathbf{x}^*) = 0$ may be solved in closed form for $\mathbf{x}^*$. In case an explicit expression for $\mathbf{g}(\mathbf{x})$ is not available, it is often approximated using semi-analytical [4] or finite difference methods [12].
(3) Second-order method: information about both $\mathbf{g}$ and $\mathbf{H}$ is employed in the optimization process. When both $\mathbf{g}$ and $\mathbf{H}$ can be evaluated directly, Newton's method is typically the most efficient optimization algorithm [12]. In case explicit expressions for $\mathbf{g}$ and/or $\mathbf{H}$ are not available, various quasi-Newton algorithms exist that employ approximations for $\mathbf{g}$ and $\mathbf{H}$ [2, 12]. The $\mathbf{H}$ matrix is commonly approximated using matrix-update methods such as the popular Broydon–Fletcher–Goldfarb–Shanno (BFGS) method [2].

A solution $\mathbf{x}^*$ is only a *local* minimum, and a highly non-linear $f(\mathbf{x})$ may possess many local minima. However, we often want to find a point where $f(\mathbf{x})$ assumes its least value, or the *global* minimum. Given an arbitrarily behaved $f(\mathbf{x})$, there is no general way to determine whether a minimum point is global or not. One strategy is to run the search algorithm as many times as possible, with each run starting from a different point. Thus the more runs, the higher chance the global minimum may be found [12].

2.1. Sensitivity analysis by indifference region

Often we are interested in finding how sensitive the model response is to variations in its parameters near an optimal point $\mathbf{x}^*$. For instance, based on such information one may devote

more effort to optimizing highly sensitive parameters, and less sensitive parameters can even be replaced by constants.

As a measure of sensitivity, we define a region within which the objective function value is only different from the optimal value by a small amount ε, i.e.

$$|f(\mathbf{x}) - f(\mathbf{x}^*)| \leqslant \varepsilon \tag{4}$$

where $||$ denotes absolute value. The collection of all $\mathbf{x}$ points that satisfy Equation (4) is referred to as the ε-*indifference region* [22]. In a sufficiently small neighbourhood of $\mathbf{x}^*$, we may approximate $f(\mathbf{x})$ by its truncated Taylor-series expansion:

$$f(\mathbf{x}) \approx f(\mathbf{x}^*) + \mathbf{g}(\mathbf{x}^*)^{\mathrm{T}}\delta\mathbf{x} + \tfrac{1}{2}\delta\mathbf{x}^{\mathrm{T}}\mathbf{H}(\mathbf{x}^*)\delta\mathbf{x} \tag{5}$$

where $\delta\mathbf{x} = \mathbf{x} - \mathbf{x}^*$. At an unconstrained minimum $\mathbf{x}^*$, $\mathbf{g}(\mathbf{x}^*) = 0$. Therefore, the indifference region can be approximated by [22]:

$$|\delta\mathbf{x}^{\mathrm{T}}\mathbf{H}(\mathbf{x}^*)\delta\mathbf{x}| \leqslant 2\varepsilon \tag{6}$$

which is the equation of an N-dimensional ellipsoid.

It is seen from Equation (6) that much information about the indifference region can be gained by analysing the Hessian matrix $\mathbf{H}(\mathbf{x}^*)$. Specifically, the size and orientation of the ellipsoid are defined by the eigenvalues and the eigenvectors of $\mathbf{H}(\mathbf{x}^*)$, respectively, [22]. Furthermore, relative sensitivities between the parameters $\mathbf{x}$ can be estimated from the shape of the ellipsoid, which is dictated by the ratios between the eigenvalues. For instance, a shorter principal axis of the ellipsoid implies that the objective function is more sensitive to the combination of parameters in that direction, and *vice versa* [22].

3. SOIL CONSTITUTIVE MODEL

The constitutive model [18] was developed based on the framework of multi-surface plasticity [23]. Herein, this model and the parameters to be optimized are briefly summarized. More details about the model can be found elsewhere [18, 19, 24, 25].

Following the classical plasticity convention [26], it is assumed that material elasticity is linear and isotropic, and that non-linearity and anisotropy result from plasticity. The selected yield function forms a conical surface in principal stress space [23], with its apex along the hydrostatic axis (Figure 1). In the context of multi-surface plasticity, a number of similar yield surfaces with a common apex and different sizes form the hardening zone (Figure 1). A modified deviatoric kinematic hardening rule was adopted [24], which dictates that all surfaces may translate in stress space within the outmost surface (failure surface).

The sizes and plastic moduli associated with the yield surfaces are typically calibrated by piecewise linearization of a non-linear shear stress–strain (backbone) curve obtained from laboratory experiments ([23], Figure 2). The backbone curve at a given reference confinement p'_{r} can be approximated by the hyperbolic formula ([27, 28], see Figure 2):

$$\tau = \frac{G\gamma}{1 + \gamma/\gamma_{\mathrm{r}}} \tag{7}$$

where τ and γ are octahedral shear stress and strain, respectively, G is the low-strain shear modulus at p'_{r} (Figure 2), and $\gamma_{\mathrm{r}} = \tau_{\max}/G$, in which $\tau_{\max}$ is the maximum shear strength when γ approaches ∞. The friction angle ϕ may be related to $\tau_{\max}$ under triaxial compression

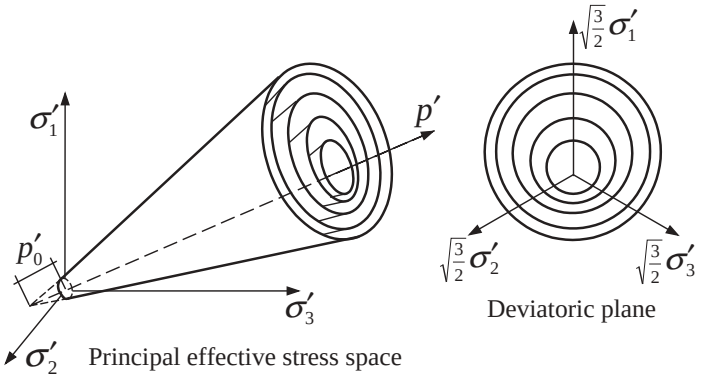

Figure 1. Employed yield surfaces in principal stress space and deviatoric plane (after Prevost [3], Parra [24] and Yang [25]).

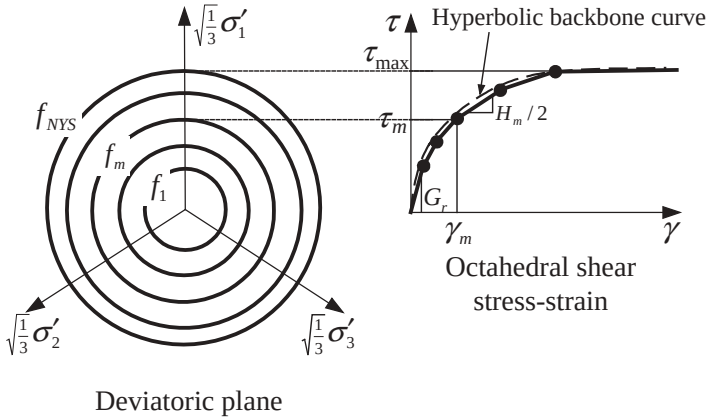

Figure 2. Hyperbolic backbone curve for soil non-linear shear stress–strain response, and piecewise-linear representation in multi-surface plasticity (after Prevost [3], Parra [24]).

conditions by [29]

$$\frac{6\sin\phi}{3-\sin\phi} = \frac{3\tau_{\max}}{\sqrt{2}p'_{\mathrm{r}}} \tag{8}$$

In this constitutive model, shear-induced contractive/dilative behaviour (dilatancy) is handled by a non-associative flow rule [24, 25]. Specifically, non-associativity is restricted to the volumetric component P'' of the plastic flow direction tensor, and the deviatoric part obeys associativity [23]. Therefore, depending on the relative location of the stress state with respect to a *phase transformation* (PT) surface [30], different expressions for P'' were specified (Figure 3(a)) for the contractive phase (when the stress state is inside the PT surface), and the dilative phase

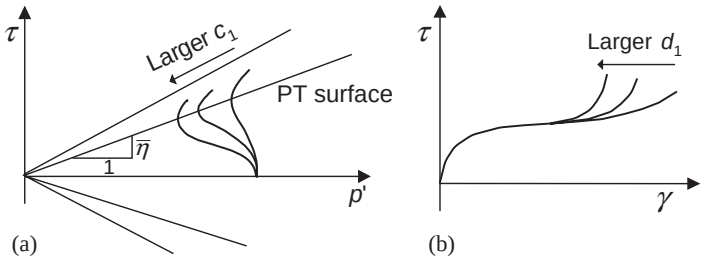

Figure 3. Effect of dilation parameters on model response: (a) dependence of confinement change (pore pressure rate) on c_1 and $\bar{\eta}$; and (b) dependence of shear stress–strain response on d_1.

during loading (outside the PT surface):

$$3P'' = \begin{cases} \dfrac{1-(\eta/\bar{\eta})^2}{1+(\eta/\bar{\eta})^2} c_1 \ (\eta < \bar{\eta}) & \text{contractive} \\ \dfrac{1-(\eta/\bar{\eta})^2}{1+(\eta/\bar{\eta})^2} d_1 \ (\eta > \bar{\eta}) & \text{dilative} \end{cases} \tag{9}$$

where η is effective stress ratio, and $\bar{\eta}$ the stress ratio along the PT surface (Figure 3(a)). The material constants c_1 and d_1 dictate the rate of contraction and dilation, respectively. Under undrained conditions, a larger c_1 results in a higher pore water pressure buildup rate (Figure 3(a)). Conversely, a larger d_1 results in stronger dilation and significantly reduces further straining (Figure 3(b)).

In the following sections, the non-linear stress–strain parameters G and γ_r (or τ_{max}) are first optimized, followed by optimization of the three dilatancy parameters c_1, d_1 and $\bar{\eta}$. Different experimental data sets and optimization techniques were employed to calibrate these two parameter groups separately. Thus, each optimization exercise only involved a smaller number of parameters, and focus could be maintained on identifying the effect of one parameter group at a time.

4. OPTIMIZATION OF NON-LINEAR SHEAR STRESS–STRAIN PARAMETERS

Results from three isotropically consolidated drained triaxial compression tests [20] were employed in optimizing the non-linear stress–strain parameters G and γ_r. These tests were conducted for 40% initial D_r, at three different confining pressures p'_r (40, 80 and 160 kPa), respectively. Since p'_r was kept constant throughout, the (octahedral) shear stress–strain response recorded during each of these tests generated a backbone curve at the corresponding p'_r. For comparison, optimization results for three additional drained triaxial compression tests conducted at 60% initial D_r are also presented.

It is noted that all test data shows a strain-softening phenomenon after maximum shear strength is reached. Since softening behaviour is not part of our modelling effort, the data points beyond the maximum shear stress were excluded. Moreover, a number of data points recorded at the initial very low levels of strain were excluded due to testing precision limitations [25].

4.1. Linear optimization

To find optimal estimates of G and γ_r, we employ the method of least squares (Equation (1)). The hyperbolic formula (Equation (7)) can be rewritten as [28]

$$\frac{\gamma}{\tau} = \frac{1}{G} + \frac{1}{\tau_{max}}\gamma \tag{10}$$

This is a linear equation in parameters $1/G$ and $1/\tau_{max}$, with γ_i/τ_i and γ_i as the experimental data set to match. Thus, the associated optimization problem is to minimize

$$f\left(\frac{1}{G}, \frac{1}{\tau_{max}}\right) = \sum_{i=1}^{N}\left(\frac{1}{G} + \frac{1}{\tau_{max}}\gamma_i - \frac{\gamma_i}{\tau_i}\right)^2 \tag{11}$$

subject to simple bounds $G > 0$ and $\tau_{max} > 0$.

Equation (11) is a simple linear optimization (regression) problem. At a minimum point (G^*, τ^*_{max}), the first derivatives of $f(1/G, 1/\tau_{max})$ vanish:

$$\frac{\partial f}{\partial(1/G)} = 2\sum_{i=1}^{N}\left(\frac{1}{G} + \frac{\gamma_i}{\tau_{max}} - \frac{\gamma_i}{\tau_i}\right) = 0, \quad \frac{\partial f}{\partial(1/\tau_{max})} = 2\sum_{i=1}^{N}\left(\frac{1}{G} + \frac{\gamma_i}{\tau_{max}} - \frac{\gamma_i}{\tau_i}\right)\gamma_i = 0 \tag{12}$$

Solving Equations (12) give the optimal values:

$$\frac{1}{\tau^*_{max}} = \frac{N\sum\gamma_i^2/\tau_i - \left(\sum\gamma_i\right)\left(\sum\gamma_i/\tau_i\right)}{N\sum\gamma_i^2 - \left(\sum\gamma_i\right)^2}, \quad \frac{1}{G^*} = \frac{\sum\gamma_i/\tau_i - (1/\tau^*_{max})\left(\sum\gamma_i\right)}{N} \tag{13}$$

Table I summarizes the optimized parameters for all six tests, along with the results from non-linear optimization to be discussed below. Note that at the same confinement level, the friction angle of the denser sand (60% D_r) is higher than that of the looser sand (40% D_r), as expected. However, the friction angle also varies with confinement for the same D_r, with the smallest value obtained at $p'_r = 80$ kPa.

A good match between the linear regression results and the experimental data is shown in Figure 4. To verify the optimization results, we perturbed the parameters G and τ_{max} in the vicinity of the optimal point and evaluated the objective function thereof (Equation (11)). In all

Table I. Summary of optimization results for non-linear shear stress–strain parameters.

		Linear optimization			Non-linear optimization			
D_r (%)	p'_r (kPa)	G (MPa)	τ_{max} (kPa)	γ_r* (%)	G (MPa)	γ_r (%)	τ_{max}* (kPa)	Friction angle† (deg)
40	40	23.36	27.35	0.117	21.61	0.125	27.01	40.3
	80	30.85	48.90	0.159	31.36	0.155	48.61	32.2
	160	43.97	109.07	0.248	44.99	0.244	109.78	35.6
60	40	26.36	31.64	0.120	24.16	0.130	31.41	41.0
	80	49.15	58.75	0.120	47.90	0.123	58.92	38.2
	160	60.32	128.90	0.214	57.28	0.226	129.45	41.7

*Calculated from $\tau_{max} = G\gamma_r$.
†Average value between linear and non-linear optimizations using Equation (8).

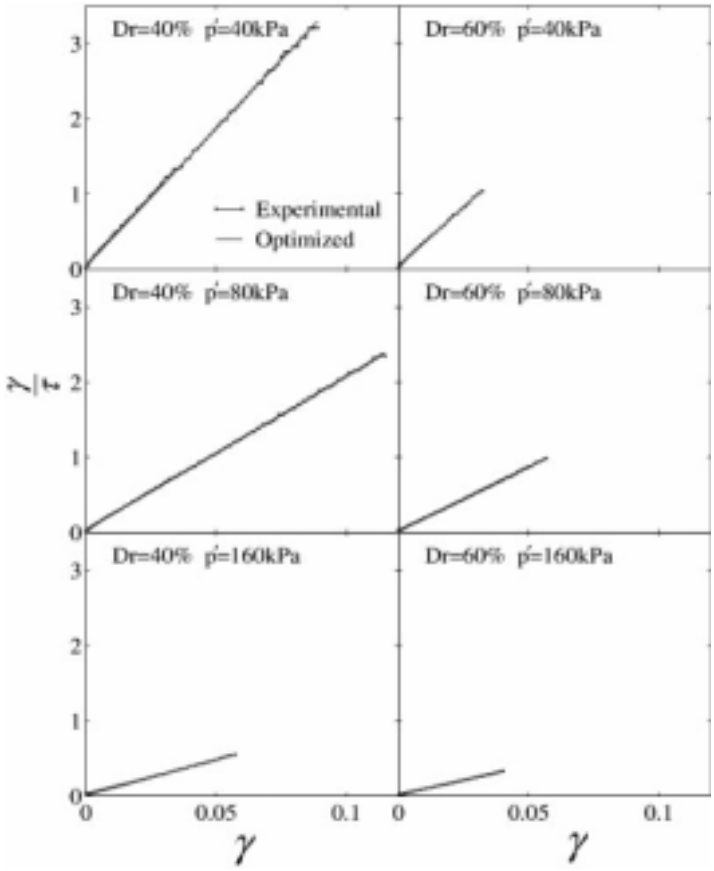

Figure 4. Experimental versus optimized (linear regression) results, showing a close match.

cases, a smooth response surface was generated (Figure 5). By examining this surface, it is clear that the optimal point is indeed a local (and actually the only) minimum.

Sensitivity analysis: In order to study parameter sensitivity, the Hessian matrix $\mathbf{H}(1/G^*, 1/\tau^*_{\max})$ (normalized by $\mathrm{diag}(G^*, \tau^*_{\max})$, Equations (3)) and its associated eigenvalues/eigenvectors were evaluated. From the results shown in Table II for the case of $D_r = 40\%$ at $p'_r = 80$ kPa, we observe that:

- Both eigenvalues of the Hessian matrix are positive. In other words, $\mathbf{H}(1/G, 1/\tau_{\max})$ is positive definite at the identified minimum point, as expected.
- The two eigenvalues are different by four orders of magnitude. This implies that, near the optimal point, the objective function is very sensitive to certain combinations of parameters and very insensitive to some other combinations [22].
- The eigenvectors define directions of extreme sensitivity or insensitivity in the space of the optimization parameters. In the present case, the extreme directions defined by the two eigenvectors nearly coincided with the two optimization parameters, indicating that the objective function is most sensitive to one parameter and least sensitive to the other.

These observations held for all six tests.

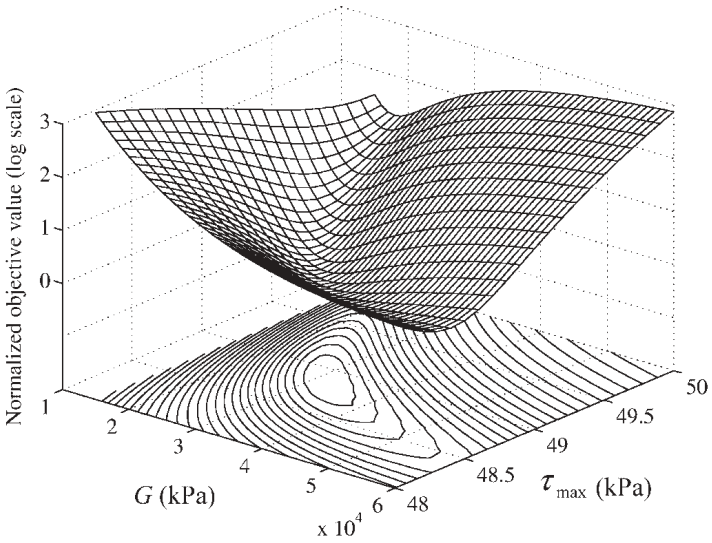

Figure 5. Typical response surface and its contour lines from linear regression (case of $D_r = 40\%$, $p' = 80$ kPa).

Table II. Normalized Hessian and associated eigenvalues/eigenvectors at the optimal point (case of $D_r = 40\%$, $p' = 80$ kPa).

	Linear regression	Non-linear optimization
Normalized Hessian	$\begin{matrix} 1/G & 1/\tau_{max} \end{matrix}$ $\begin{bmatrix} 1.292 \times 10^{-7} & 4.234 \times 10^{-6} \\ 4.234 \times 10^{-6} & 2.052 \times 10^{-4} \end{bmatrix}$	$\begin{matrix} G & \tau_{max} \end{matrix}$ $\begin{bmatrix} 2.346 \times 10^{5} & 2.239 \times 10^{5} \\ 2.239 \times 10^{5} & 2.148 \times 10^{5} \end{bmatrix}$
Eigenvalues	4.184×10^{-8}, 2.052×10^{-4}	4.488×10^{5}, 5.547×10^{2}
Eigenvectors	$\begin{bmatrix} 0.9998 \\ -0.0206 \end{bmatrix}$ $\begin{bmatrix} 0.0206 \\ 0.9998 \end{bmatrix}$	$\begin{bmatrix} -0.7226 \\ -0.6913 \end{bmatrix}$ $\begin{bmatrix} 0.6913 \\ -0.7226 \end{bmatrix}$

The 10%-indifference region ($|f(\mathbf{x}) - f(\mathbf{x}^*)| \leqslant 0.1|f(\mathbf{x}^*)| = \varepsilon$) was estimated for each test (using Equation (6)). As shown in Figure 6 (note different scales on the horizontal and vertical axes), $f(\mathbf{x})$ is very sensitive to the parameter τ_{max}, with less than 1.0% change in τ_{max} causing 10% change in the objective value. This confirms the last two observations about the Hessian matrix above.

Finally, to examine the quality of the indifference region approximated by $\mathbf{H}(1/G, 1/\tau_{max})$, the actual contour of the 10%-indifference region was obtained from the response surface (Figure 5) and drawn in Figure 6. In general, good agreement between the actual and the estimated 10%-indifference regions is seen for all cases.

4.2. Non-linear optimization

Alternatively, Equation (7) can be employed for optimization directly, with the objective function defined to be the difference between calculated and experimental shear stresses at the

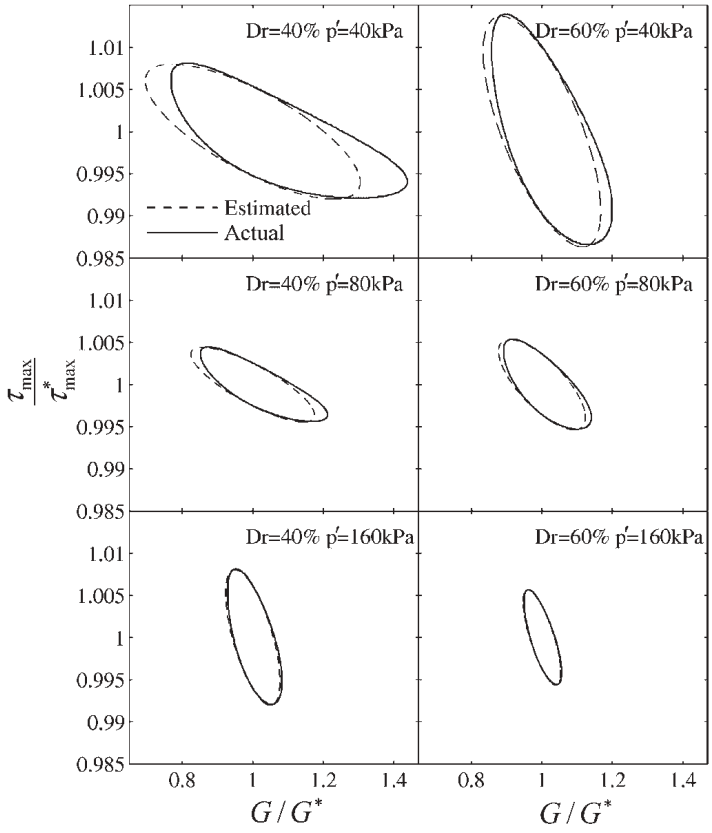

Figure 6. Actual versus estimated 10% indifference region from linear regression (different scales on horizontal and vertical axes for clarity).

same strain levels:

$$f(G, \gamma_r) = \sum_{i=1}^{N} \left(\frac{G\gamma_i}{1 + \gamma_i/\gamma_r} - \tau_i \right)^2 \tag{14}$$

subject to $G > 0$ and $\gamma_r > 0$. At a minimum point, the first derivatives vanish:

$$\frac{\partial f}{\partial G} = 2 \sum_{i=1}^{N} \left(\frac{G\gamma_i}{1 + \gamma_i/\gamma_r} - \tau_i \right) \frac{\gamma_r \gamma_i}{\gamma_r + \gamma_i} = 0, \quad \frac{\partial f}{\partial \gamma_r} = 2 \sum_{i=1}^{N} \left(\frac{G\gamma_i}{1 + \gamma_i/\gamma_r} - \tau_i \right) \frac{G\gamma_i^2}{(\gamma_r + \gamma_i)^2} = 0 \tag{15}$$

The above equations are non-linear in G and γ_r, and cannot be solved in closed form. One has to resort to a numerical optimization algorithm. As **g** and **H** can be evaluated analytically in this case, we employed Newton's method.

For each of the six cases, different starting points were selected when applying Newton's method. It turns out that multiple solutions (i.e. multiple local minima) exist. However, only one solution satisfies the physical bounds ($G > 0$ and $\gamma_r > 0$). Table I summarizes the optimization results, revealing good agreement with those from the linear optimization. Comparison of the non-linear optimization (and linear regression) results with the experimental data is shown in Figure 7.

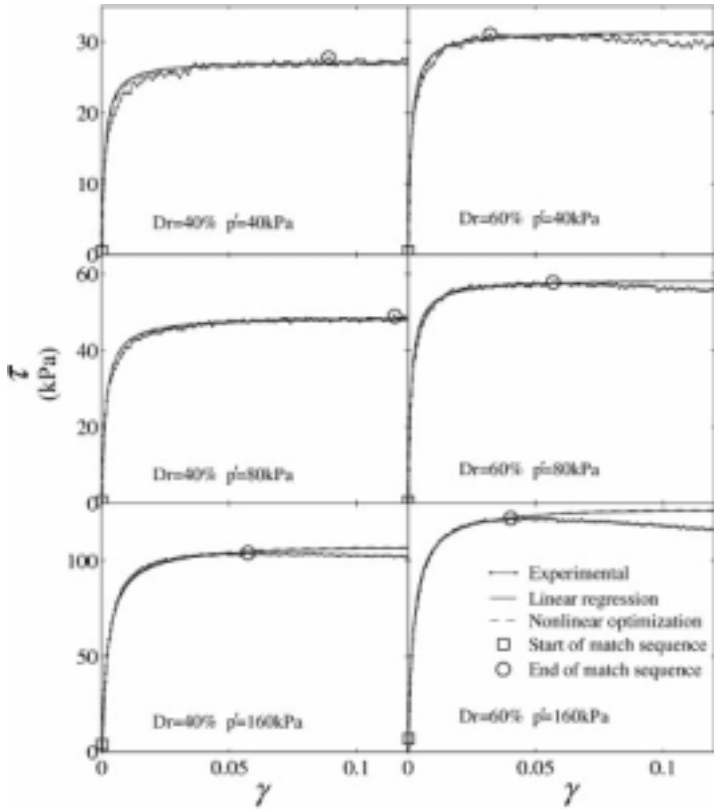

Figure 7. Measured and optimized octahedral shear stress–strain curves of drained monotonic triaxial tests.

Sensitivity analysis: The estimated 10%-indifference regions (Equation (6)) are shown in Figure 8. Comparisons between the estimated and the actual indifference regions show excellent agreement. Finally, the Hessian matrix (normalized by $\mathrm{diag}(1/G^*, 1/\gamma_r^*)$) at the optimal point for the case of $D_r = 40\%$ at $p'_r = 80$ kPa is included in Table II, with the two eigenvalues differing by three orders of magnitude. This large difference between the eigenvalues is also demonstrated by the severely elongated shape of the indifference regions (Figure 8).

Note that the shapes of the indifference regions in the linear and non-linear optimization cases are correlated due to $\tau_{max} = G\gamma_r$. Hence, if τ_{max} is a sensitive parameter (Figure 6), so is the product $G\gamma_r$ (Figure 8).

Confinement dependence of G: In practice, confinement dependence of the shear modulus G for sand is typically expressed by a power law with a power coefficient of 0.5, i.e. $G_1 = G(p'_1/p'_r)^{0.5}$ [31]. This relationship is drawn in Figure 9 for $D_r = 40$ and 60%, respectively. In the case of $D_r = 40\%$, the power-law expression shows a rather good agreement with the optimized G at all three confinement levels. However, some discrepancy is seen between the power-law prediction and the optimized values in the case of $D_r = 60\%$.

Remark

Optimization of G and γ_r was performed either analytically (first-order method) or by using the simple Newton's method (second-order method), since the objective function is smooth and the

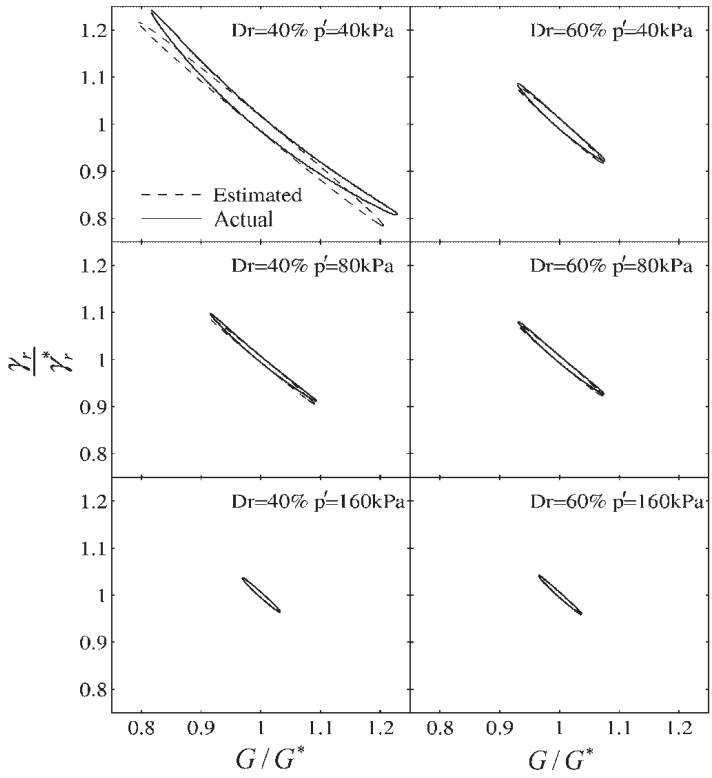

Figure 8. Actual versus estimated 10% indifference region from non-linear optimization.

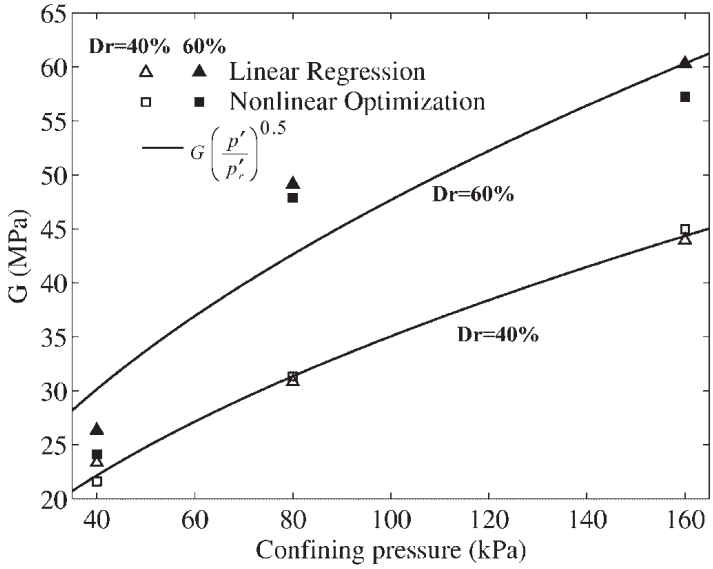

Figure 9. Dependence of shear modulus on confining pressure.

gradients are easy to evaluate. In the following section, optimization of the dilatancy parameters will be conducted for 40% D_r Nevada sand, with G and γ_r fixed at the optimal values (case of $p'_r = 80$ kPa). In this case, each evaluation of the objective function is done through a non-linear dynamic FE simulation, and $\mathbf{g}(\mathbf{x})$ and $\mathbf{H}(\mathbf{x})$ cannot be computed directly. Therefore, a more elaborate numerical optimization approach is adopted.

5. OPTIMIZATION OF DILATANCY PARAMETERS

The dilatancy parameters (Equation (9)) are calibrated by matching the results of a dynamic centrifuge test conducted at Rensselaer Polytechnic Institute [21, 32]. This test (VELACS Model 2) was a 1D site-response simulation of a prototype stratum of 10 m depth and infinite lateral extent (Figure 10), under nearly harmonic base excitation (0.2 g peak acceleration at predominantly 2 Hz frequency, [21]). The model represents a mildly inclined slope, with an effective inclination angle of about 4°. The same Nevada sand employed in the drained triaxial tests above was used in this experiment, at an initial D_r of about 40%.

During the test, soil response along the model profile was monitored, including pore pressure transducers (PPTs), lateral displacement sensors (LVDTs), and lateral accelerometers (Figure 10). It was observed that (Figures 11 and 12): (1) liquefaction reached about 5 m depth, and (2) cycle-by-cycle accumulation of permanent lateral displacement occurred at all monitored locations, with the maximum surface displacement reaching 0.47 m. The results of this test were thoroughly documented by Taboada [32], and further analysed in References [15, 18, 21].

In order to carry out the calibration, the constitutive model was incorporated in a 2D plane-strain, solid–fluid fully coupled finite element (FE) program [33]. This program was used in conjunction with an existing numerical optimization code SNOPT [34] for optimization and sensitivity studies of the dilatancy parameters. Figure 10 shows the FE mesh employed for the

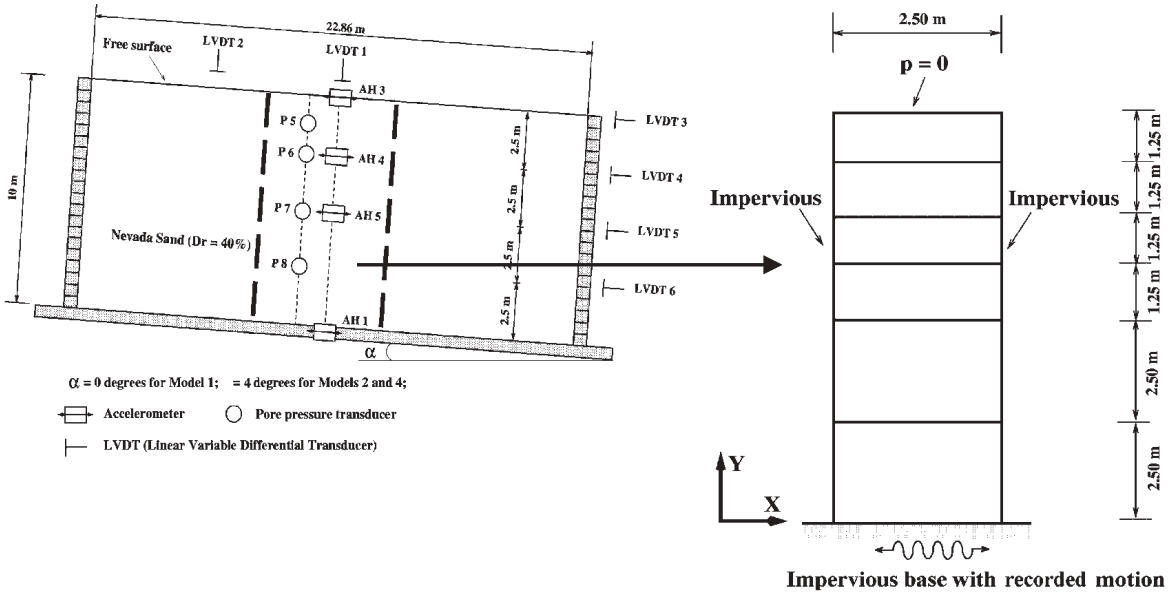

Figure 10. VELACS Model 2 centrifuge configuration [21, 32] and employed finite element mesh.

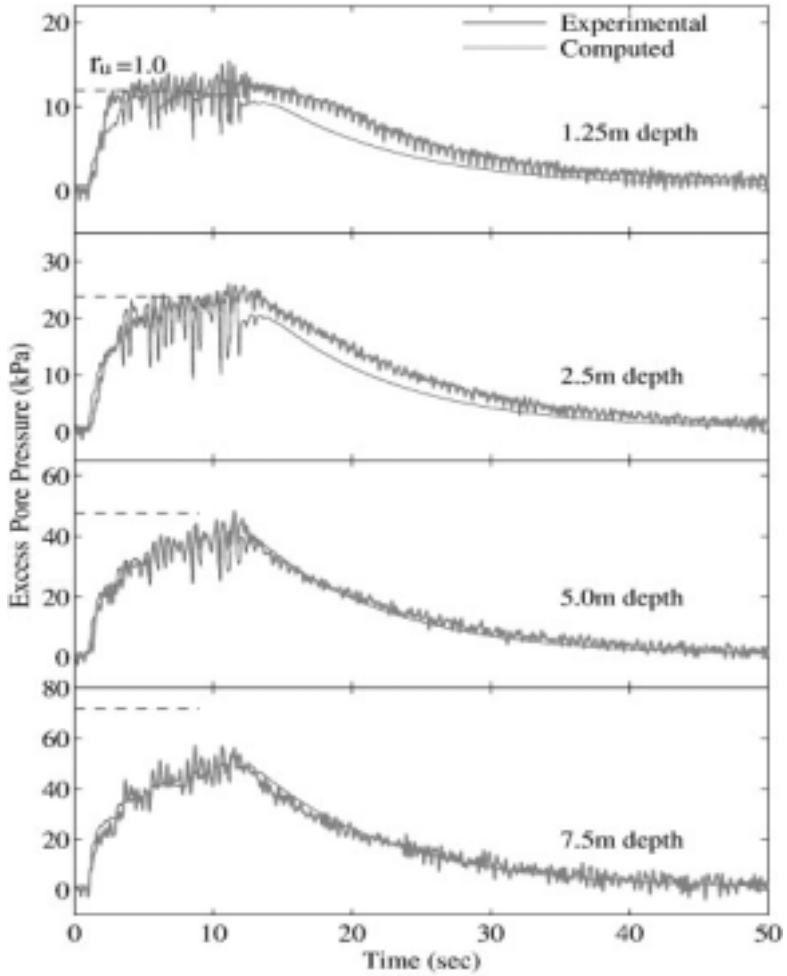

Figure 11. VELACS model 2 optimized versus recorded [32] excess pore pressure history at all monitored locations ($r_u = u_e/\sigma'_v$ where σ'_v is initial effective vertical confinement).

numerical simulations (see Reference [18] for more details regarding the numerical modelling procedures).

5.1. *Definition of objective function*

An appropriate definition of objective function is crucial to a successful optimization exercise. Given various response quantities measured from an experiment, it is important to identify and include in the objective function the quantities of relevance to the model parameters being optimized. This subset of experimental data may include different response variables, measured at different locations and/or time windows. Even within the selected data set, different weighing factors can be assigned to different parts, in proportion to their perceived relative significance in the overall optimization problem.

In our current study, excess pore pressure (u_e) and lateral displacement are of direct relevance to the model dilatancy parameters being optimized. It is obvious that the rate of u_e build-up

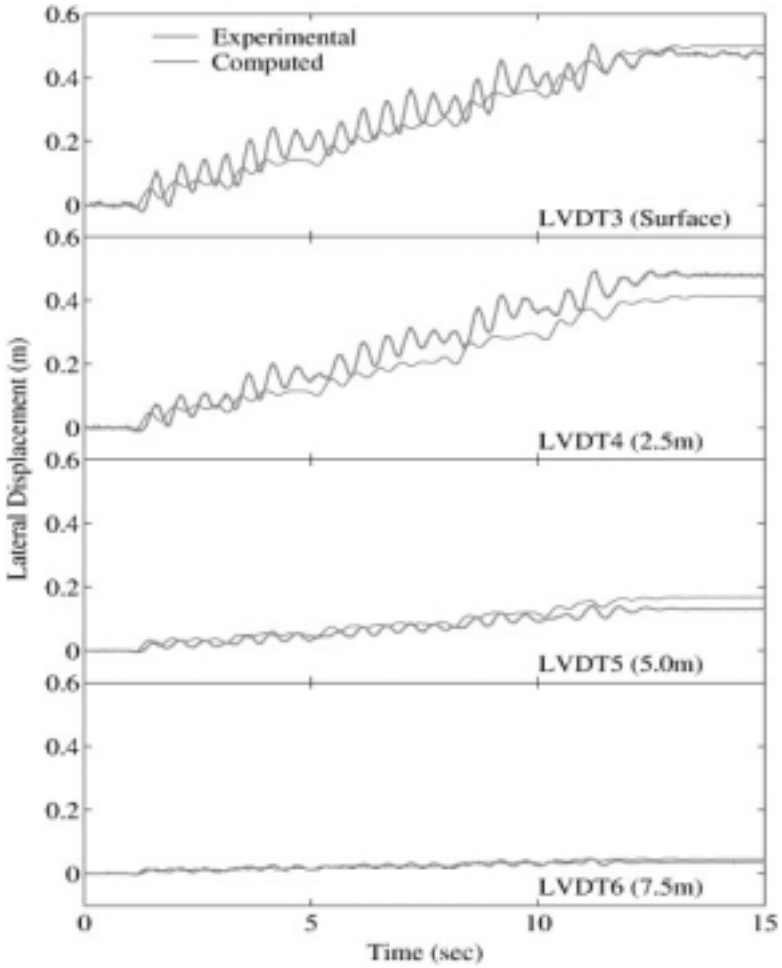

Figure 12. VELACS model 2 optimized versus recorded [32] lateral displacement history at all monitored locations.

during the shaking phase was dictated directly by the contraction parameter c_1, as well as $\bar{\eta}$ (Figure 3(a)). On the other hand, the extent of permanent lateral displacement accumulation depends largely on [18] the post-liquefaction dilation tendency (dictated mainly by d_1, Figure 3(b)). Based on these considerations, the objective function was defined to be the sum of squared errors (Equation (1)) in computed u_e and lateral displacement responses at all monitored (PPT and lateral LVDT) locations (Figure 10), i.e.

$$f(c_1, d_1, \bar{\eta}) = \sum_{t=0}^{T} \left[\sum_{i=1}^{4} (u_e(t,i) - \tilde{u}_e(t,i))^2 + W \sum_{j=1}^{4} (d(t,j) - \tilde{d}(t,j))^2 \right] \tag{16}$$

in which $u_e(t,i)$ and $\tilde{u}_e(t,i)$ are recorded and computed excess pore pressure at time t and PPT location i, respectively, $d(t,j)$ and $\tilde{d}(t,j)$ are recorded and computed lateral displacement at time t and LVDT location j, respectively, and W is a weighing factor such that the two response

Table III. Summary of numerical optimization results for dilatancy parameters.

Run No. and bounds	Initial value				Final value			
	c_1	d_1	$\bar{\eta}/\eta_f$	$f(x)^*$	c_1	d_1	$\bar{\eta}/\eta_f$	$f(x)^*$
1	0.17	0.4	0.844	1.472	0.211	1.317	0.84	1.0
2	0	0	0.955	37.90	0.207	2.873	0.897	1.095
3	0	0	0.478	37.31	0.351	0.283	0.478	1.047
4	0	0	0.844	37.82	0.194	0.922	0.843	1.033
Lower bound	0.0	0.0	0.4					
Upper bound	3.0	30.0	0.955					

*All objective values are normalized by the optimal objective value of the first run.

quantities (u_e and d) contribute equally (approximately) to the objective function magnitude. Moreover, reasonable lower and upper bounds were set for all optimization parameters (Table III), based on previous modelling experience. For simplicity, acceleration response was not included in the optimization.

5.2. Numerical optimization program

For this study, an existing numerical optimization program, SNOPT, was employed. SNOPT [34] is a general-purpose system for solving optimization problems, developed jointly at the Department of Mathematics, U.C. San Diego and the Department of Management Science and Engineering, Stanford University. SNOPT minimizes a linear or non-linear function that may involve many variables and (linear or non-linear) constraints. A Sequential Quadratic Programming (SQP) technique is adopted in SNOPT, in which the search for an optimal point is advanced at each step by minimizing a quadratic model of the objective function and associated constraints. SQP is a second-order method with each QP subproblem solved using the BFGS quasi-Newton method. Unspecified gradients (by the user) are approximated by finite difference. SNOPT finds solutions that are *locally* optimal. A major advantage of SNOPT is that it requires relatively fewer evaluations of the objective function [34]. In our current application, each such evaluation is done through a time-consuming dynamic FE simulation. Hence, this code was quite efficient for our purposes.

5.3. Optimization results

A total of four optimization runs were conducted with each run starting at a different initial point (Table III), in order to cover a broader range of possible parameter combinations. The results are summarized in Table III ($\bar{\eta}$ normalized by stress ratio of the failure surface, η_f). Note that each optimization run approached a different optimal point (i.e. the solution is not unique), though the final objective function values were very close. The non-uniqueness of solution stems from the highly non-linear nature of the objective function, as the computed response time histories were generated from an FE program with strong non-linearity and complicated logic. The 'best' calibrated u_e and lateral displacement results (solution No. 1 in Table III) are depicted in Figures 11 and 12, respectively, showing a reasonable agreement with the experimental counterparts. The computed versus recorded lateral acceleration results are also shown in Figure 13 (not part of the objective function as mentioned above).

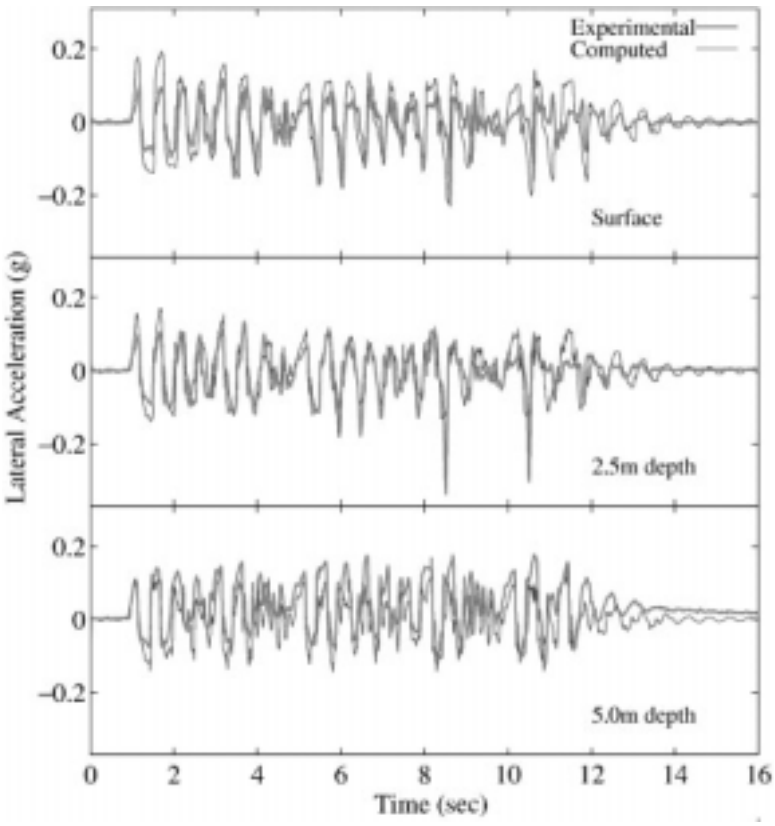

Figure 13. VELACS model 2 computed versus recorded [32] lateral acceleration history at all monitored locations.

A closer inspection of the four solutions in Table III reveals the interrelation of the optimization parameters. Specifically, a lower optimal value for $\bar{\eta}$ (solution No. 3) corresponded to higher c_1 but lower d_1 values, and *vice versa* (solution No. 2). During shear loading, a lower $\bar{\eta}$ (Figure 3(a)) results in reduced contraction and increased dilation. Thus, in order to match the recorded level of u_e build-up within a shorter period of time, a stronger contraction tendency (i.e. higher c_1 value) was necessary. On the other hand, higher d_1 combined with lower $\bar{\eta}$ values would have resulted in excessive dilation (Figure 3(b)), with less accumulated lateral displacement (shear strain) compared to the experimental data.

To further appreciate this interplay between optimization parameters, the combined effect of d_1 and $\bar{\eta}$ on the objective function was evaluated (with c_1 fixed at the calibrated value) as shown in Figure 14. Indeed, it is seen that higher d_1 combined with lower $\bar{\eta}$ values (or lower d_1 with higher $\bar{\eta}$) caused the objective function value to increase. However, there exists a large indifference region near the global minimum (shaded area in Figure 14), within which perturbations of d_1 and $\bar{\eta}$ do not result in appreciable increase in the objective value. However, due to the rough texture of the response surface (Figure 14), identification of such a region is a difficult task. In particular, characterizing this region by pointwise $\mathbf{H}(\mathbf{x})$ information may lead to significant error. On the other hand, including additional experimental data in the objective function might help reduce this region.

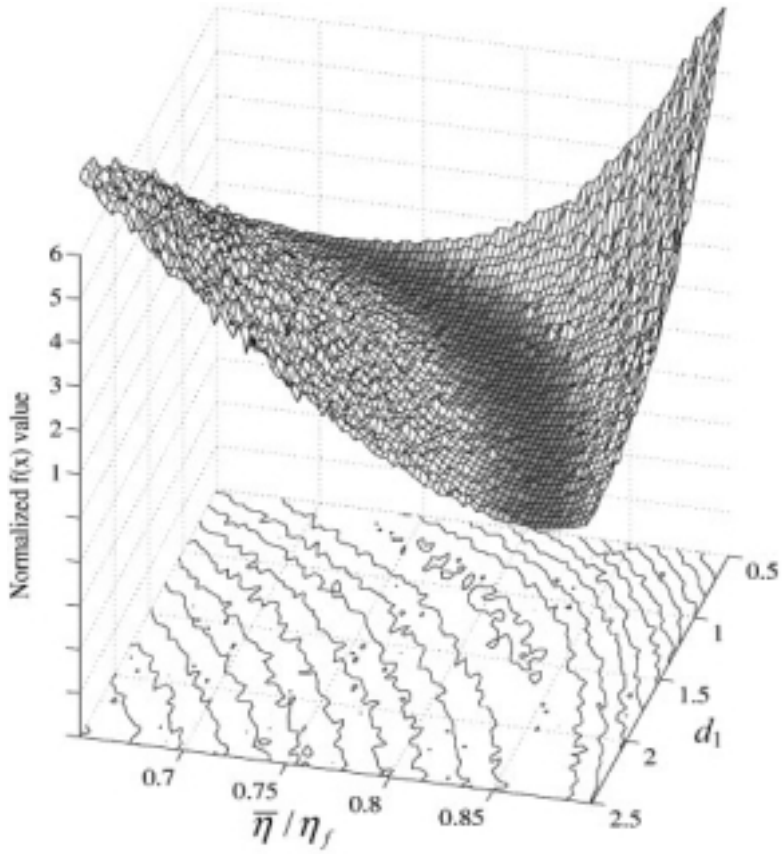

Figure 14. Response surface and its contour lines for independent variables d_1 and $\bar{\eta}$.

5.4. *Parameter sensitivity study*

To check the quality of the calibration results (solution No. 1, Table III), the optimized dilation parameters were perturbed individually (with all others fixed at the corresponding optimal values) at the vicinity of the calibrated values, and the corresponding objective function was evaluated. The resulting response curves shown in Figure 15 assume a similar pattern: the objective function reaches a region of low values near the calibrated parameter values, and increases as the parameters move away from the calibrated values. This demonstrates that: (1) the calibrated parameter values are effective in reducing the objective value, and (2) the objective function is reasonably sensitive to all three dilatancy parameters near the optimal point. Furthermore, it is observed that all response curves are highly non-linear, with many local minima. This characteristic of the objective function is mainly responsible for the non-unique results from the different optimization runs (Table III).

Finally, the convergence performance of the optimization algorithm is shown in Figure 16, in terms of the number of objective function evaluations. In most cases, significant reduction in objective function value was achieved at an early stage of the optimization process, and difficulty increased as the (local) optimal point was gradually approached.

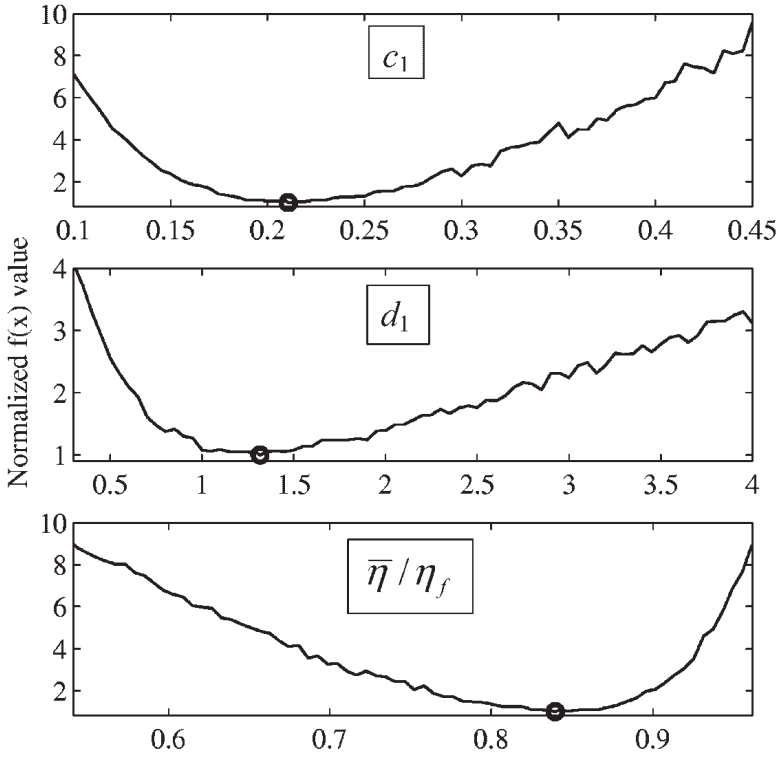

Figure 15. Sensitivity of objective function to optimization parameters.

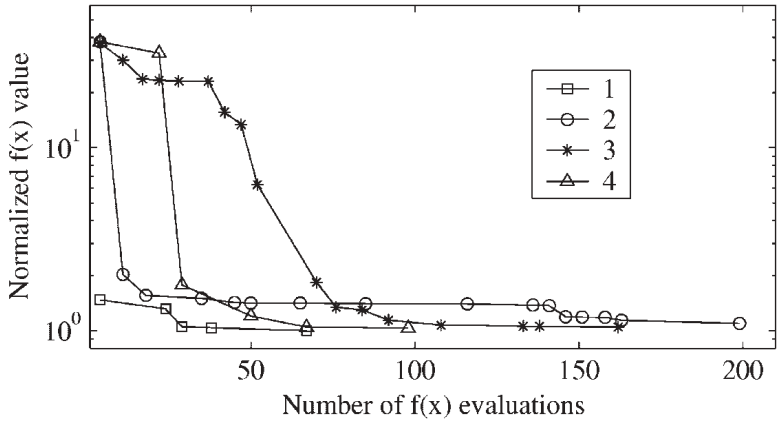

Figure 16. Convergence rate of numerical optimizations in terms of number of objective function evaluations.

6. SUMMARY AND CONCLUSIONS

The current study aims to explore different optimization techniques for systematic calibration of soil constitutive models. Three optimization methods (analytical, semi-analytical and numerical) were employed to calibrate a multi-surface plasticity model for 40% D_r Nevada sand. The model

non-linear shear stress–strain behaviour was first calibrated by analytical and semi-analytical methods, based on results from a set of drained triaxial sample tests. Thereafter, the dilatancy parameters were calibrated using an existing numerical optimization code (SNOPT), based on results from a dynamic centrifuge test.

The following conclusions can be drawn from this study:

1. The prerequisite for a meaningful optimization exercise is that the theoretical model must adequately capture the physical mechanisms that are responsible for the observed essential response characteristics. Moreover, an appropriate objective function should include observation data of significant relevance to the model parameters being optimized.
2. When multiple mechanisms are included in a theoretical model, it is often possible to perform optimization on a subgroup of the model parameters associated with just one mechanism, based on the experimental data mainly representing this mechanism. A major advantage of this approach is that each optimization exercise only involves a smaller number of parameters, and focus can be maintained on identifying the effect of one mechanism at a time.
3. Applicability of various optimization techniques depends largely on the availability and complexity of the first and second gradients of the objective function. Analytical or semi-analytical methods should be employed when the gradients are available and easy to compute. Otherwise, one has to resort to a more advanced numerical algorithm.
4. Sensitivity analyses provide critical information about the relative importance of each parameter. For a sufficiently smooth objective function, parameter sensitivity may be estimated by studying the Hessian matrix at the optimal point. However, this method may not be applicable to highly non-linear objective functions.
5. Results from optimization analyses and associated sensitivity studies are based only on the data included in the objective functions, and are subject to change when more data is available. In this sense, an optimization process can be viewed as an evolving process, rather than a one-time exercise.

ACKNOWLEDGEMENTS

This work was supported by the National Science Foundation (Grant No. CMS-9416248), and the Pacific Earthquake Engineering Research (PEER) Center, under the National Science Foundation Award Number EEC-9701568. The authors are grateful to Professor Philip Gill of the Department of Mathematics at U.C. San Diego, for sharing the SNOPT software package and valuable discussions. Dr K. Arulmoli (Earth Mechanics) graciously provided the triaxial testing data. Professor Ricardo Dobry (RPI) and Professor Victor Taboada (UNAM) graciously provided the centrifuge testing data. This assistance is greatly appreciated.

REFERENCES

1. DeNatale JS. On the calibration of constitutive models by multivariate optimization. *Ph.D. Dissertation*, University of California, Davis, 1983.
2. Abifadel N, Klisinski M, Sture S, Ko HY. Unconstrained optimization for the calibration of an elasto-plastic constitutive model. *Report*, Department of Civil, Environmental, and Architectural Engineering, University of Colorado, Boulder: U.S. Army Engineer Waterways Experiment Station, Contract DACA 39-83-C-0012, 1988; 65.
3. Zeghal M, Abdel-Ghaffar AM. Identification of the behavior of earth dams using seismic records. *Report No*. CRECE 9001, Center for Research in Earthquake Engineering and Construction, University of Southern California, September 1989.

4. Anandarajah A, Agarwal D. Computer-aided calibration of a soil plasticity model. *International Journal for Numerical and Analytical Methods in Geomechanics* 1991; **15**(12):835–856.
5. Klisinski M, Abifadel N, Runesson K, Sture S. Modelling of the behavior of dry sand by an elasto-plastic 'Fuzzy Set' model. *Computers and Geotechnics* 1991; **11**:229–261.
6. Mattsson H, Klisinski M, Axelsson K. Optimization routine for identification of model parameters in soil plasticity. *International Journal for Numerical and Analytical Methods in Geomechanics* 2001; **25**(5):435–472.
7. Zeghal M, Oskay C. A local identification technique for geotechnical and geophysical systems. 2003; *International Journal for Numerical and Analytical Methods in Geomechanics* 2003; **27**(11):967–987.
8. Rosenbrock HH. An automatic method for finding the greatest or least value of a function. *Computer Journal* 1960; **3**:175–184.
9. Powell MJD. An efficient method for finding the minimum of a function of several variables without calculating derivatives. *Computer Journal* 1964; **7**:155–162.
10. Fletcher R. *Practical Methods of Optimization-Volume I: Unconstrained Optimization*. Wiley: Chichester, UK, 1980.
11. Fletcher R. *Practical Methods of Optimization-Volume II: Constrained Optimization*. Wiley: Chichester, UK, 1981.
12. Gill PE, Murray W, Wright MH. *Practical Optimization*. Academic Press: London, 1981.
13. Dennis JE, Schnabel RB. *Numerical Methods for Unconstrained Optimization and Non-linear Equations*. Prentice-Hall: Englewood Cliffs, NJ, 1983.
14. Zeghal M. System identification of the nonlinear seismic response of earth dams. *Ph.D. Thesis*, Princeton University, NJ, 1990.
15. Elgamal AW, Zeghal M, Taboada VM, Dobry R. Analysis of site liquefaction and lateral spreading using centrifuge model tests. *Soils and Foundations* 1996; **36**(2):111–121.
16. Zeghal M, Abdel-Ghaffar A-M. Evaluation of the nonlinear seismic response of earth dams: I. Pattern recognition. 2003; in review.
17. Zeghal M, Abdel-Ghaffar A-M. Evaluation of the nonlinear seismic response of earth dams: II. System identification. 2003; in review.
18. Elgamal A, Yang Z, Parra E. Computational modeling of cyclic mobility and post-liquefaction site response. *Soil Dynamics and Earthquake Engineering* 2002; **22**(4):259–271.
19. Yang Z, Elgamal A, Parra E. A computational model for cyclic mobility and associated shear deformation. *Journal of Geotechnical and Geoenvironmental Engineering*, ASCE 2003; **129**(12).
20. Arulmoli K, Muraleetharan KK, Hossain MM, Fruth LS. VELACS: verification of liquefaction analyses by centrifuge studies. *Laboratory Testing Program, Soil Data Report*, The Earth Technology Corporation, Project No. 90-0562, Irvine, CA, 1992.
21. Dobry R, Taboada VM. Possible Lessons from VELACS Model No. 2 Results. *Proceedings, the International Conference on the Verification of Numerical Procedures for the Analysis of Soil Liquefaction Problems*, Arulanandan K, Scott RF (eds), vol. 2. Balkema, Rotterdam, 1994; 1341–1352.
22. Bard Y. *Nonlinear Parameter Estimation*. Academic Press: New York, 1974.
23. Prevost JH. A simple plasticity theory for frictional cohesionless soils. *Soil Dynamics and Earthquake Engineering* 1985; **4**(1):9–17.
24. Parra E. Numerical modeling of liquefaction and lateral ground deformation including cyclic mobility and dilation response in soil systems. *Ph.D. Thesis*, Department of Civil Engineering, Rensselaer Polytechnic Institute, Troy, NY, 1996.
25. Yang Z. Numerical modeling of earthquake site response including dilation and liquefaction. *Ph.D. Dissertation*, Department of Civil Engineering and Engineering Mechanics, Columbia University, New York, NY, 2000.
26. Hill R. *The Mathematical Theory of Plasticity*. Oxford University Press: London, 1950.
27. Kondner RL. Hyperbolic stress–strain response: cohesive soils. *Journal of Soil Mechanics and Foundations Division*, ASCE 1963; **89**(SM1):115–143.
28. Duncan JM, Chang CY. Nonlinear analysis of stress and strain in soils. *Journal of Soil Mechanics and Foundations Division*, ASCE 1970; **96**(SM5):1629–1653.
29. Chen WF, Mizuno E. 1990. *Nonlinear Analysis in Soil Mechanics, Theory and Implementation*. Elsevier: New York, NY.
30. Ishihara K, Tatsuoka F, Yasuda S. Undrained deformation and liquefaction of sand under cyclic stresses. *Soils and Foundations* 1975; **15**(1):29–44.
31. Seed HB, Idriss IM. Soil moduli and damping factors for dynamic response analyses. *Report* EERC 70-10, Earthquake Engineering Research Center, University of California, Berkeley, 1970.
32. Taboada VM. Centrifuge modeling of earthquake-induced lateral spreading in sand using a laminar box. *Ph.D. Thesis*, Rensselaer Polytechnic Institute, Troy, NY, 1995.
33. Yang Z, Elgamal A. Influence of permeability on liquefaction-induced shear deformation. *Journal of Engineering Mechanics*, ASCE 2000; **128**(7):720–729.
34. Gill PE, Murray W, Saunders M. SNOPT: An SOP algorithm for large-scale constrained optimization. *Report NA 97-2*, Department of Mathematics, University of California, San Diego, *Report* SOL 97-3, Department of EESOR, Stanford University, 1997.

